ACCSCIENCE PUBLISHING

International Journal of Bioprinting

RESEARCH ARTICLE

3D-printed degradable hair follicular hanging-drop scaffolds integrated with tissue-engineered skin promote hair follicle regeneration *in vitro*

Bin Yao[1,2,3†], Yuhong Wang[1,2†], Dongzhen Zhu[4†], Tian Hu[5], Sha Huang[4*], and Ping Zhu[1,2*]

[1]Guangdong Cardiovascular Institute, Guangdong Provincial People's Hospital (Guangdong Academy of Medical Sciences), Southern Medical University, Guangzhou, Guangdong, China

[2]Guangdong Provincial Key Laboratory of Pathogenesis, Targeted Prevention and Treatment of Heart Disease, Guangzhou Key Laboratory of Cardiac Pathogenesis and Prevention, Guangzhou, Guangdong, China

[3]Academy of Medical Engineering and Translational Medicine, Tianjin University, Tianjin, China

[4]Research Center for Tissue Repair and Regeneration Affiliated to the Medical Innovation Research Department, PLA General Hospital and PLA Medical College, Beijing, China

[5]MRC Human Immunology Unit, MRC Weatherall Institute of Molecular Medicine, University of Oxford, Oxford, United Kingdom

[†]These authors contributed equally to this work.

***Corresponding authors:**
Ping Zhu
(tanghonggdph@163.com)

Sha Huang
(stellarahuang@sina.com)

Citation: Yao B, Wang Y, Zhu D, Hu T, Huang S, Zhu P. 3D-printed degradable hair follicular hanging-drop scaffolds integrated with tissue-engineered skin promote hair follicle regeneration *in vitro*. *Int J Bioprint*. 2025;11(2):412-428. doi: 10.36922/ijb.8535

Received: January 14, 2025
1st revised: February 7, 2025
2nd revised: February 18, 2025
Accepted: February 19, 2025
Published Online: February 19, 2025

Copyright: © 2025 Author(s). This is an Open Access article distributed under the terms of the Creative Commons Attribution License, permitting distribution, and reproduction in any medium, provided the original work is properly cited.

Publisher's Note: AccScience Publishing remains neutral with regard to jurisdictional claims in published maps and institutional affiliations.

Abstract

Currently, a substantial number of patients suffer from the distress of skin defects. Tissue-engineered skin represents a promising alternative therapeutic option for these patients. However, the currently available tissue-engineered skin products still exhibit significant limitations, including poor long-term viability and a lack of appendages. The advent of three-dimensional (3D) printing technology and organoid formation techniques provides a promising avenue for addressing these challenges. In this study, we constructed a scaffold using 3D printing with sodium alginate (NaAlg)/gelatin (GEL)/alginate lyase hydrogel, which has controllable pore size and degradation rate. This scaffold provides a favorable microenvironment for the colonization and functional maturation of hair follicular hanging drops within artificially organized skin. *In vitro* observations revealed the regeneration of hair follicles and the high expression of hair follicle-specific markers, LIM homeobox 2 (LHX2), and cytokeratin 17 (CK17). In addition, we studied the follicular polarization of the engineered skin compared to normal skin and attempted to identify possible underlying mechanisms. In conclusion, our findings present a novel strategy for establishing artificial skin with appendages.

***Keywords*:** 3D bioprinting; Alginate lyase; Hair follicle; Microenvironment; Skin appendage regeneration

1. Introduction

Annually, a substantial number of patients suffer from severe skin loss or disfigurement caused by trauma, chronic diseases, or dermatological conditions.[1-3] The skin is a complex organ that can heal after extensive damage. However, it cannot regenerate

appendages such as sweat glands and hair follicles. The loss of these structures results in impaired thermoregulation, reduced barrier function, and emotional distress, which significantly impacts the patient's quality of life.[4,5] The current clinical equivalents for wound repair are limited to the simple dermis and epidermis layers or solely the dermis layer. These approaches lack the capacity to promote regeneration of skin appendages.[6–8] Accordingly, there is a substantial clinical need for the development of an artificial skin substitute that incorporates sweat glands and hair follicles.

Tissue-engineered skin offers a promising alternative therapy for these patients and can provide an *in vitro* drug screening platform for many skin diseases.[9–12] However, currently available tissue-engineered skin still has significant limitations, including poor long-term viability and a lack of appendages, which play a role in thermoregulation, barrier function, and wound healing.[4,11,13] In recent years, an increasing number of researchers have focused on this research priority. Lei et al.[14] developed an *in vitro* culture condition that forms skin organoids from isolated cells and allows organoid explants to form skin with normal hair structures. Abaci et al.[15] used computer-aided 3D printing technology to plant human hair papillae with epidermal cells in tissue-engineered skin, achieving the regeneration of human hair tissue *in vitro*. Huang et al.[16,17] used microcarriers and 3D printing technology to construct tissue-engineered skin containing sweat glands *in vitro* and used it for wound sweat gland regeneration. Kang et al.[18] demonstrated that intradermal delivery of hair follicle dermal cell spheroids promoted hair follicle regeneration in nude mice. In addition, mixtures of isolated neonatal mouse epidermal and dermal cells forming hair follicle hanging drops have also been reported to differentiate into hair follicles *in vitro* and integrate into engineered skin.[14,19] Although many studies have reported advances in the construction of appendages *in vitro*, existing methods are complex, time-consuming, and remain a challenge for the development of tissue-engineered skin with functional and structural appendages and their large-scale dissemination.

The aim of this study was to develop a tissue-engineered skin via 3D printing technology that is simple to construct, scalable on a large scale, and supports polarized hair follicle growth. We use NaAlg/gelatin (GEL)/alginate lyase composite hydrogels to construct scaffolds with controlled pore size and degradation rate to provide a microenvironment for hair follicular hanging-drop colonization and functional maturation within artificial tissue skin. Meanwhile, we further investigated the potential mechanisms underlying the polarized growth of hair follicles in normal skin. Compared to conventional approaches, single-cell sequencing offers unique advantages in delineating cell–cell interactions and gene regulatory networks, thereby providing novel strategies for engineering artificial skin with functional appendages (Scheme 1).

2. Materials and methods

2.1. Materials

High-glucose Dulbecco's Modified Eagle Medium (DMEM) was purchased from Hyclone (United States of America [USA]). Fetal bovine serum (FBS) was obtained from GIBCO (USA). Trypsin-EDTA and a mixture of penicillin/streptomycin were procured from Solaibao Biotechnology Co., Ltd (China). GEL, sodium alginate, alginate lyase, collagenase I, and Dispase neutral protease were all acquired from Sigma (USA). Goat serum was sourced from ZSJQ-BIO (China). Reverse transcription polymerase chain reaction (RT-PCR) and quantitative RT-PCR (qRT-PCR) kits were purchased from Takara (China). Live/dead assays kit (NO. C2015S), 4% paraformaldehyde solution (NO. P0099-100ml), 0.3% Triton X-100 (NO. P0096-100ml), 3% bovine serum albumin (BSA; NO. P0268-100ml), and Cell Counting Kit-8 (CCK8; NO. C0037) were purchased from Beyotime (China).

C57BL/6J mice and Sprague-Dawley (SD) rats were obtained from Huafukang Biological Technology Co., Ltd (China). All animal experiments were approved by the Animal Ethics Committee of Tianjin University (TJUE-2024-515) and adhered to the guidelines of the Chinese Association for Laboratory Animal Science.

2.2. Mechanical properties

Compositions of 1% NaAlg and 1% NaAlg/3% GEL were configured and cast into rectangular molds measuring 10 × 8 × 2 mm^3. The inks were crosslinked for 24 h using 300 mg/mL of calcium chloride. Prior to testing, the samples were placed in a 37 °C oven for 1 h to ensure that GEL was sacrificed.

The photocrosslinked hydrogels were carefully placed on the platform of a universal testing machine (INSTRON, USA).[20] For testing, the maximum displacement was set at half of the initial thickness of the specimen, and the compression rate was controlled at 0.05 mm/s. This method allowed the stress–strain (S–S) curve to be calculated for each specimen. This standardized test procedure was applied to each experimental group with at least three replications ($n = 3$) to ensure the reliability and reproducibility of the data obtained.

2.3. Biocompatibility of bioinks

A bioink containing 3% GEL, 1% NaAlg, and 0.5 mU/mL sodium alginate lyase was configured. Subsequently, 300

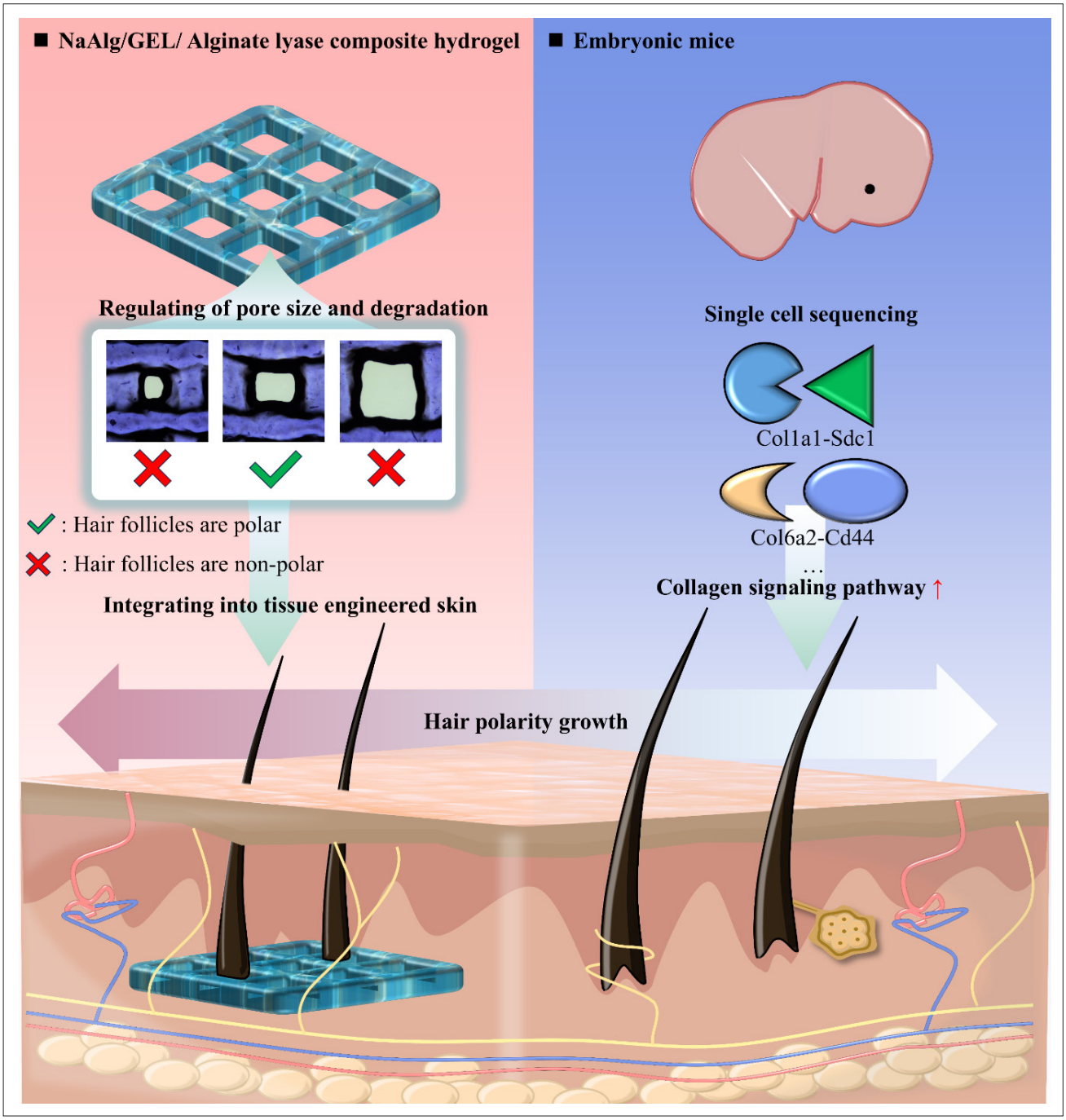

Scheme 1. 3D-printed degradable hair follicular hanging-drop scaffolds integrated with tissue-engineered skin promote hair follicle polarity growth similar to that of normal skin. Abbreviation: GEL, gelatin.

mg/mL calcium chloride was then added for crosslinking for 10 min. Phosphate-buffered saline (PBS) was used for two rinses to remove excess calcium chloride. The crosslinked bioink was then co-incubated with complete DMEM medium, which was used directly to culture L929 cells. Live/dead assays were performed on Days 3 and 5 of the culture period. Calcein AM and propidium iodide (PI) were diluted with Dulbecco's Phosphate-Buffered Saline (DPBS) to final concentrations of 2 and 8 μM, respectively. At each time point, DPBS was washed twice, and the calcein AM/PI mixture was then added. After incubation at 37 °C for 25 min under light-free conditions, imaging

was performed using a microscope (Nikon, Japan), and semiquantitative analysis was performed using ImageJ software. Cell survival was calculated by dividing the number of live cells by the total number of cells counted.

The CCK8 concentrate was diluted 10-fold in DMEM/F12 medium and used as the working solution. The assay was performed on Days 3 and 5 of cell culture by rinsing the cells twice with PBS, then adding the CCK8 working solution and incubating at 37 °C for 30 min. Absorbance was measured using a microplate reader at 450 nm. A blank group of CCK8 working solution without cells was set up to account for background absorbance, and the value of the blank group was subtracted from each experimental group.

2.4. Fibroblast isolation and culture

After euthanizing neonatal mice within 24 h of birth, the surface skin was disinfected twice. On ice, the skin of the mice was completely cut off, and the dermal side of the skin was placed face down on the surface of 0.25% trypsin solution and left overnight at 4 °C. Subsequently, the epidermis was removed, and the dermal tissue was placed in a centrifuge tube containing DMEM complete culture medium, with 2 mL of a 3.5 mg/mL type I collagenase solution added per mouse dermis, followed by incubation at 37 °C in a water bath with low-speed shaking for 40 min. After the shaking was completed, 20 mL of DMEM complete culture medium was added to the dermis of each mouse. All liquids were passed through a 40 μm cell strainer and then centrifuged (150 × *g*, 5 min). The cells were resuspended using DMEM complete culture medium and plated in culture dishes. After 60 min, the medium was changed to remove non-adherent contaminating cells. At this point, the cells obtained were fibroblasts.

2.5. Epidermal cell isolation and culture

After euthanizing neonatal mice within 24 h of birth, the surface skin was disinfected twice. On ice, the skin of the mice was completely cut off, and the dermal side of the skin was placed face down on the surface of 0.25% trypsin solution and left overnight at 4 °C. Subsequently, the dermis was removed, and the epidermal tissue was placed in a clean culture dish, to which 1–2 mL of complete culture medium and trypsin were added. Using sterile surgical scissors, the epidermis was minced, and the minced tissue and liquid were transferred to a 15 mL centrifuge tube, quickly inverted up and down 10–15 times. The processed tissue and liquid were passed through a 40 μm cell strainer, and after filtration, the liquid was centrifuged at 1500 rpm for 5 min. The sediment after centrifugation consisted of epidermal cells.

2.6. Preparation of hair follicular hanging drops

Following the method reported in Lei et al.,[14] freshly isolated neonatal dermal fibroblasts and epidermal cells were mixed in a ratio of fibroblasts to epidermal cells of 9:1. On the underside of a culture dish lid, 20 μL droplets of DMEM complete culture medium were pipetted, and 1–1.5 μL of the mixed dermal–epidermal cell suspension was then added to the interior of each droplet. The lid was then placed upside down on a culture dish containing 10 mL of sterile PBS and placed in a cell incubator at 37 °C for 48 h. At this point, the cellular clumps within each droplet constitute the hair follicular hanging drops.

2.7. Extraction and purification of rat tail collagen

The tails of SD rats were removed, retaining only the tail tendons. The tendons were placed in a Tris-HCl-NaCl buffer solution and soaked for 24 h before mincing. Then, 50 mL of pepsin was added, and the solution was stirred at low speed at 4 °C for 72 h. Subsequently, the solution was centrifuged at 5000 × *g* for 20 min at 4 °C, and the supernatant was collected. Approximately, 2 mol/L NaCl salting-out solution was added to the supernatant, centrifuged at 5000 × *g* for 20 min at 4 °C, and the precipitate was collected. The collected precipitate was then dissolved using 0.1 mol/L acetic acid solution and placed in a dialysis bag for dialysis in pure water for 3 days to obtain purified rat tail collagen.

2.8. Skin tissue engineering

Following the method previously described,[21] concentrated DMEM, FBS, and sodium bicarbonate solution were mixed in rat tail collagen in the appropriate ratios and spread over the upper chamber of a transwell to form a cell-free collagen layer at room temperature for 15 min. Then, a dermal cell suspension at a concentration of 1×10^6 cells/mL was added to the rat tail collagen, along with concentrated DMEM, FBS, and sodium bicarbonate solution. This mixture was placed on top of the already solidified cell-free collagen layer and incubated at 37 °C for 30 min. After incubation, complete DMEM culture medium was added, and the mixture was cultured for 7 days to form the dermal layer. After incubation, the culture medium above the dermal layer was removed and incubated at room temperature for 20 min. An epidermal cell suspension at a concentration of 1×10^7 cells/mL was prepared and mixed with 50 μL of the epidermal cell suspension on top of each dermal layer at room temperature for 15 min, before further incubation for 60 min to ensure complete adhesion of the epidermal cells. The epidermal layer I culture medium was added to cover the entire tissue and cultured for 4 days, with the medium changed every 2 days. After the 4-day culture, the medium was switched to the epidermal

layer II culture medium and further cultured for 2 days. Finally, the culture medium was removed from the upper chamber; the keratinization culture medium was added to the lower chamber to form an air–liquid interface and cultured for 2 additional days, with the medium changed every 2 days.

2.9. 3D printing of guiding scaffolds

2.9.1. Preparation of bioink

A mixed solution containing 3% (w/v) GEL and 1% (w/v) NaAlg was prepared using deionized water. The prepared bioink was placed in a 70 °C water bath for 30 min, then cooled in a 4 °C refrigerator for 5 min. This process was repeated three times to sterilize the bioink. Prior to printing, the bioink was heated to 37 °C until it was completely liquid; alginate lyase was then added to give a final concentration of 0.5 mU/mL. Subsequently, 500 μL of fibroblast cell suspension was added to every 10 mL of bioink, resulting in a final cell density of 1×10^6 cells/mL in the bioink.

2.9.2. 3D printing process

The prepared cell-laden bioink was transferred into the printing cartridge (Bio-Architect PRO; Regenovo Co., China), and the sealed cartridge was placed in a 15 °C cold water bath for 15 min. The printer parameters were set as follows: the print head temperature at 15 °C, the platform temperature at 4 °C, the printing speed at 7–14 mm/s, and the printing pressure at 0.07–0.12 MPa. The 3D model dimensions were set to $30 \times 30 \times 3$ mm^3. After printing, the printed constructs were immersed in different concentrations of calcium chloride solution for crosslinking, depending on the requirements of the experiment. After crosslinking for 10 min, the crosslinking agent was removed; the constructs were washed twice with complete culture medium, added with complete culture medium, and placed in a 37 °C incubator for 1 h, before another change of the medium. Finally, for long-term culture, the medium was changed every 2 days.

2.10. Hematoxylin and eosin staining

The frozen sections were placed at room temperature for 15 min, washed twice with PBS, stained with hematoxylin for 7 min, and then rinsed with water. The sections were quickly dipped once in the differentiation solution and subsequently rinsed with water; quickly immersed once in the bluing reagent and rinsed with water; stained with eosin for 1 min and rinsed once with water; and quickly immersed twice in 80% ethanol, followed by dehydration in 95% and anhydrous ethanol for 1 min each. Finally, the sections were treated with xylene for 2 min and then mounted with resin.

2.11. Single-cell RNA-sequencing analysis

Raw sequence data for E13.5 and E14.5 mouse skin was obtained from the NCBI GEO database (accession no. GSE122043, https://www.ncbi.nlm.nih.gov/gds/?term=GSE122043).[22] The Seurat software package (version 5.0.3) was utilized for downstream analyses, including quality control, data integration, cell type identification, and differential gene expression analysis. Cells were filtered based on the following criteria: number of detected genes (500 < nFeature_RNA < 7000), percentage of mitochondrial gene expression (mt_percent < 20%), percentage of hemoglobin gene expression (HB_percent < 5%), and total RNA counts (1000 < nCount_RNA < 97th percentile). To address batch effects arising from biological replicates in each group, the Harmony package was employed for data integration.

After integration, the data were scaled using the ScaleData function, and principal component analysis (PCA) was performed using the RunPCA function, retaining the first 30 principal components (dims = 1:30) for downstream analyses. Unsupervised clustering was conducted with the FindNeighbors and FindClusters functions, using a resolution parameter of 0.3. To identify marker genes specific to each cluster, the FindAllMarkers function was applied with thresholds set to an average log2 fold change (avg_log2FC > 0.25) and an adjusted *p*-value (p_val_adj < 0.05). Identified marker genes were used to assign cell types to clusters based on known gene expression patterns.

Cell–cell communication across cell types was analyzed using the CellChat R package (version 1.6.1), which infers interactions based on ligand–receptor pairs from the CellChatDB database. The compute Commun Prob Pathway function was employed to infer cell–cell communication at the signaling pathway level. Communication probabilities were calculated by summing the probabilities of related ligand–receptor pairs, thereby quantifying interaction strength.

2.12. Statistical analysis

All data are presented as the mean ± standard deviation. Statistical significance was analyzed using Student's *t*-test, and a *p*-value of less than 0.05 was considered to indicate a statistically significant difference.

3. Results and discussion

3.1. Fabrication of 3D-printed degradable hair follicular hanging-drop scaffolds

Although the hair-inducing capacity of hair follicular hanging drops has been extensively documented in the literature, integrating hair follicles into tissue-engineered skin remains a challenge.[23,24] Our previous work revealed

that using conventional tissue engineering methods, whether placing hair follicular hanging drops on the surface or the bottom of tissue-engineered skin, the lack of appropriate spatial constraints prevents the development of hair follicular hanging drops into hair fibers. Moreover, the absence of a scaffold leads to random growth of hair follicles, which is detrimental to the formation of tissue-engineered skin with fully functional appendages (Figure 1a).

NaAlg, a natural polysaccharide, is widely used in the field of biomedical engineering due to its excellent biocompatibility and gel-forming ability.[22–28] In this study, we introduced alginate lyase into the alginate bioink to regulate the degradation rate of the alginate-based bioink.

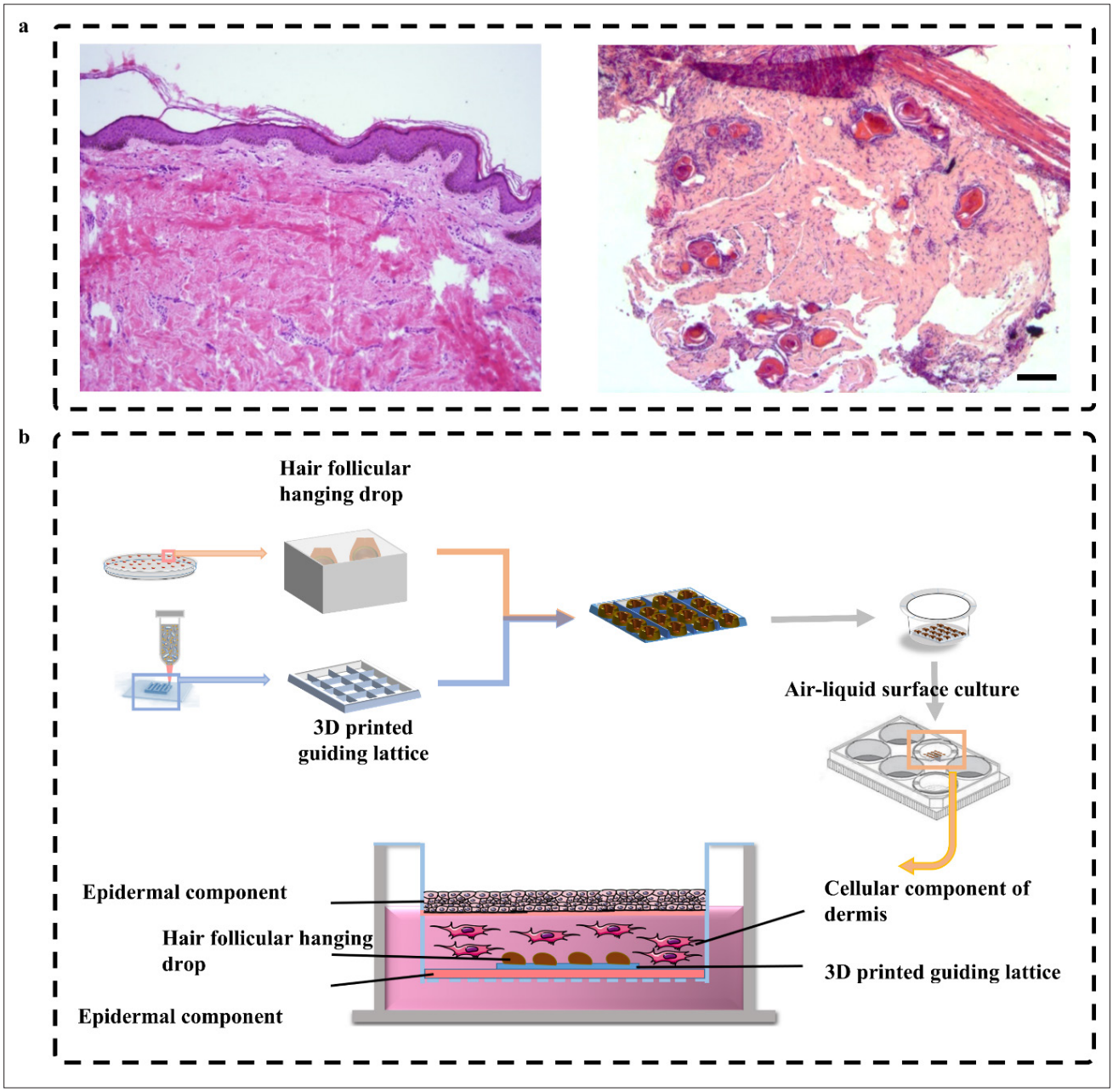

Figure 1. Tissue-engineered skin constructed by traditional methods compared with engineered-skin integrated with 3D-printed degradable hair follicular hanging-drop scaffolds. (a) Hematoxylin and eosin (HE)-stained sections of tissue-engineered skin constructed using conventional methods (left image: hair papilla cells; right image: intermediate hair follicle). Scale bar: 1 mm. (b) Construction process of a 3D-printed degradable hair follicular hanging-drop scaffold.

The lyase gradually degrades the molecular network formed by the crosslinking of alginate molecules, leading to changes in porosity and hardness. This is considered to be the primary factor influencing the behavior of cells within the bioink.[29,30] When the molecular network is hard and the porosity is low, cells within the bioink do not have sufficient space to move. Meanwhile, the application of 3D printing technology in constructing tissue-engineered skin offers numerous advantages, particularly in terms of size and structural controllability. The scaffold plays a key role in establishing the microenvironment necessary for the survival of skin appendages, and the structure of these scaffolds directly affects the structure and function of skin appendages, such as hair follicles and sweat glands.[31,32] A well-designed scaffold can mimic the native extracellular matrix, providing not only mechanical support but also biochemical signals essential for cell behavior. Figure 1b demonstrates the construction of a 3D-printed biodegradable hair follicular hanging-drop scaffold.

3.2. Physical properties of bioinks and construction of 3D-printed degradable hair follicular hanging-drop scaffolds

To improve the printability of sodium alginate, we added 3% GEL to the bioink. Based on our previous findings, a bioink composed of 3% GEL and 1% NaAlg exhibits excellent printability and biocompatibility.[33] After crosslinking with calcium chloride, gelatin can be removed by increasing the temperature (Figure 2a). After GEL was sacrificed, we found that the mechanical strength of the remaining sodium alginate was similar to that of sodium alginate without gelatin (Figure 2b). Additionally, the addition of low concentrations of alginate lyase has minimal impact on the overall stiffness, porosity, and physical properties of the bioink.[33] For visualization purposes, we mixed the bioink with trypan blue dye before printing. To better align with the size of the hair follicular hanging drops, three distinct types of degradable scaffolds, each featuring unique pore sizes, were specifically designed. These scaffolds are illustrated in Figure 2c. The overall photographs and microscopic structures of the printed scaffolds presented in the figure demonstrate that the bioink system can maintain the developmental scaffold required by the hair follicles. The pore size of the scaffold is crucial for the formation and function of hair follicles.[34,35] Pore sizes that are too small may restrict cell proliferation and nutrient exchange, while pores that are too large may fail to guide the physiological growth pattern of hair follicles. Therefore, determining the optimal pore size is essential for promoting the healthy development of hair follicles and ensuring the proper integration of hair follicles with surrounding tissues.

3.3. Degradation time and biocompatibility of 3D-printed degradable hair follicular hanging-drop scaffolds

In tissue engineering, particularly in skin regeneration, the degradation rate of the scaffold is a critical consideration.[36] Ideally, the degradation of the scaffold should be synchronized with the timeline of skin repair. If the scaffold degrades too quickly, the newly formed tissue may lack sufficient structural support; conversely, if it degrades too slowly, it may hinder the natural healing process, leading to complications such as fibrosis. Since the main components of tissue-engineered skin are collagen and fibroblasts, the 3D scaffold must degrade within a certain period after being implanted into the tissue-engineered skin. Our previous work has demonstrated that different concentrations of crosslinking agents not only affect the hardness and porosity of the bioink but also its degradation time. We set up crosslinking agents with different concentrations of calcium chloride and observed their degradation after the same crosslinking time. As displayed in Figure 3a–c, the 150 mg/mL calcium chloride crosslinking group began to exhibit degradation under the microscope on the third day of culture, and the gross structure disintegration was observed on the fifth day of culture. The 300 mg/mL calcium chloride crosslinking group began to exhibit structural loosening under the microscope after 5 days of culture. We set up a gradient of different concentrations, including 75, 150, 300, and 600 mg/mL of crosslinking agents; we observed the degradation of the printed structures under the microscope and from a gross perspective and plotted the quantification graph ($p < 0.05$). Subsequently, we selected a crosslinking agent concentration of 300 mg/mL as the experimental condition for subsequent experiments, as the degradation time of this group's structure was similar to the *in vitro* culture time of the tissue-engineered skin.

In addition, in order to verify whether the 3D-printed biodegradable scaffold and its degradation products are cytotoxic, we co-cultured the biodegradable scaffold with L929 cells. On the third and fifth day of co-culture, we found that the activity of the cells was above 90% and continued to proliferate, which proved that the scaffold had good biocompatibility (Figure 3d–f).

3.3. Pore size of the scaffold regulates the growth direction and structure of hair follicles

To better simulate the microenvironment for hair follicle growth, we transplanted hair follicular hanging drops that had formed for 24 h onto the printed degradable scaffolds and then integrated them onto the acellular collagen layer (dermis) (Figure 4a and b). The *in vitro* skin model was cultured normally according to the methods for tissue-engineered skin. After 3 days of culture, we examined

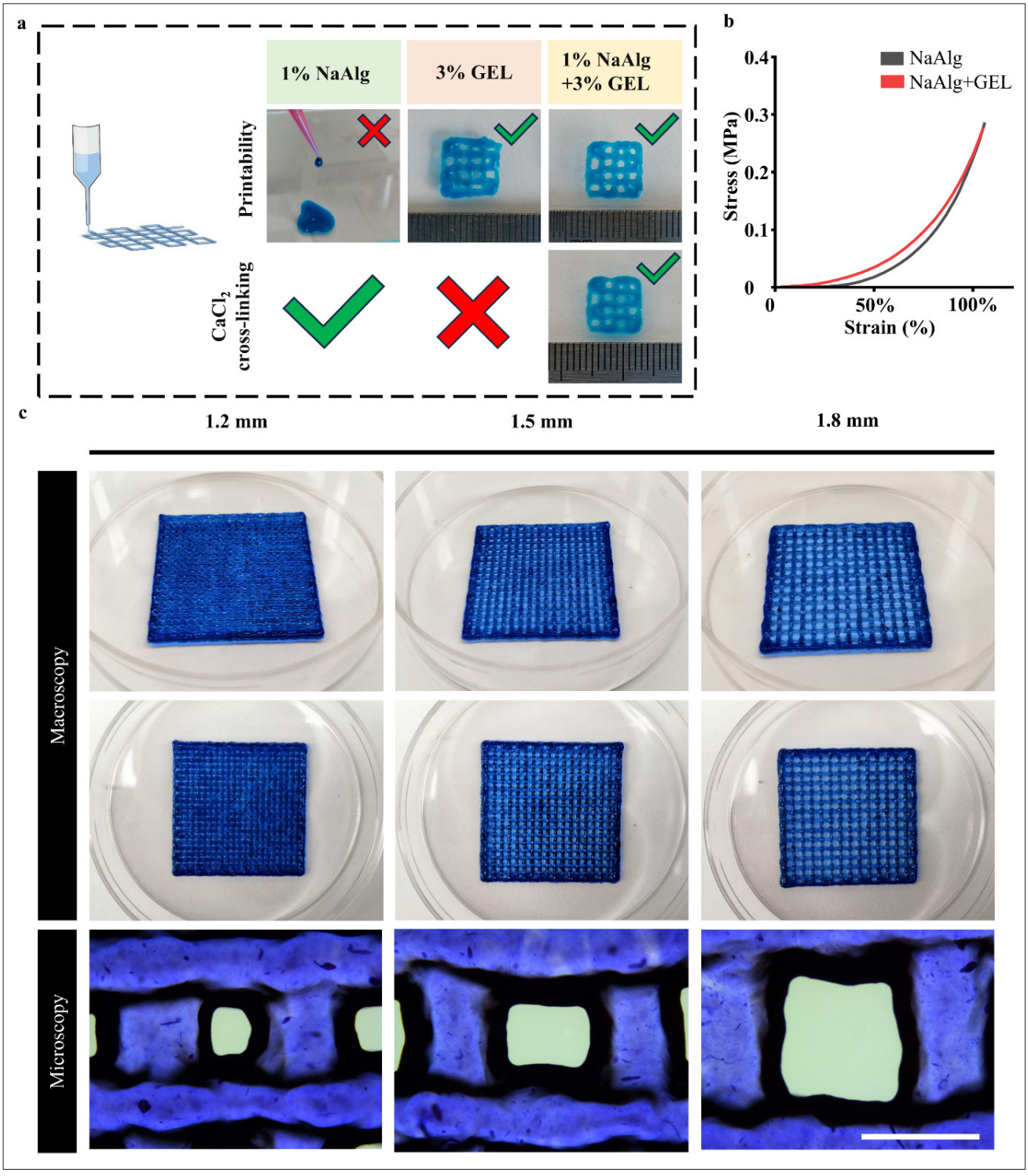

Figure 2. Characteristics and design of 3D-printed degradable hair follicular hanging-drop scaffolds of the guiding lattice. (a) Printability of bioinks. (b) Stress–strain curves of bioinks. (c) Three types of scaffolds were printed with axial distances between the pores of 1.2, 1.5, and 1.8 mm, respectively. Scale bar: 1 mm. Abbreviation: GEL, gelatin.

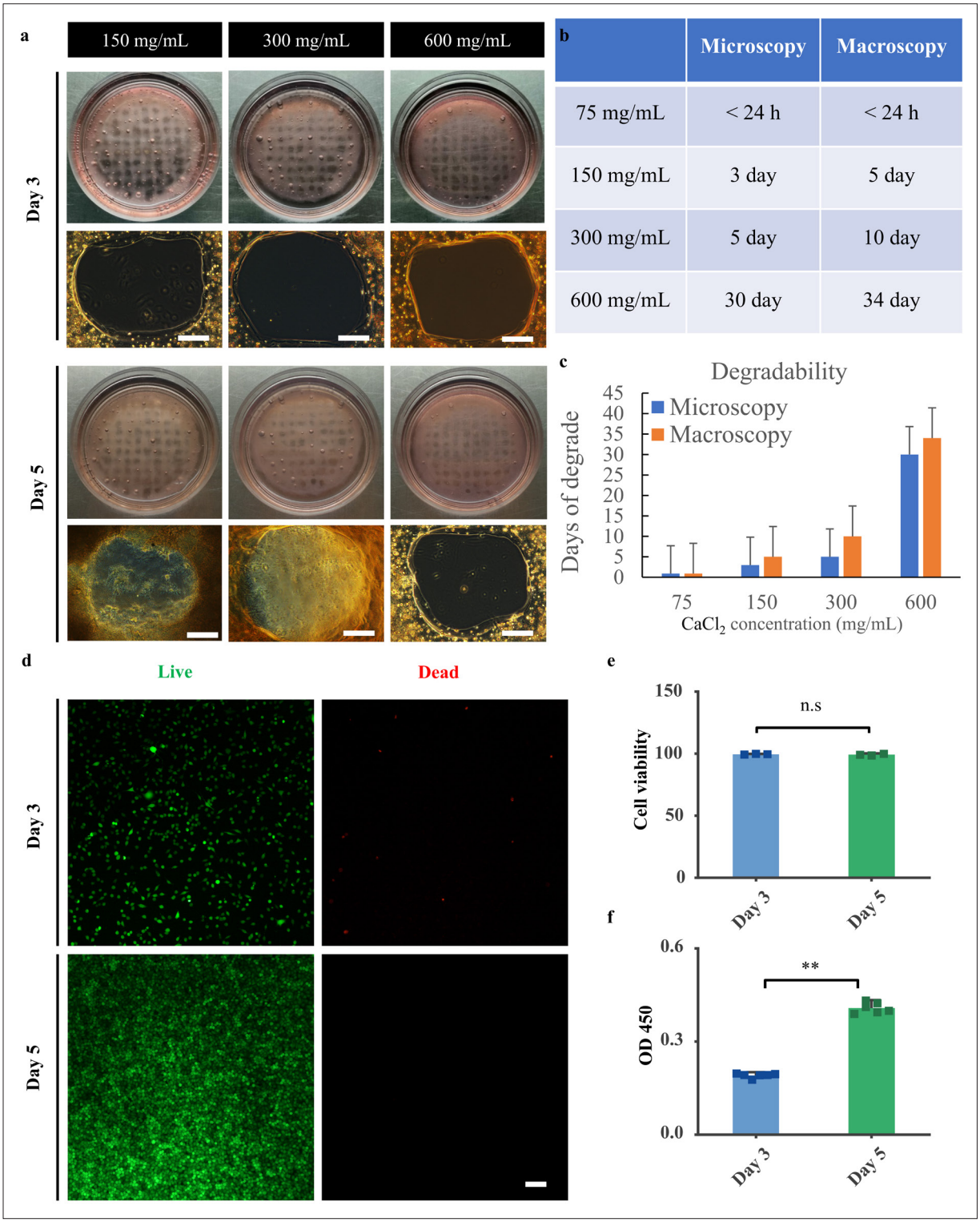

Figure 3. The effect of different concentrations of crosslinking agents on the degradation of printed structures. (a) Macroscopic and microscopic structural images of printed structures cultured in vitro for three and five days with three concentrations of crosslinking agents. Scale bars: 500 μm. (b) Degradation timeline for macroscopic and microscopic structures with four concentrations of crosslinking agents. (c) Bar chart of degradation times for macroscopic and microscopic structures with four concentrations of crosslinking agents (n = 3). (d) Live/dead fluorescent images of l929 cells. Scale bar: 100 μm. (e) Semi-quantitative analysis based on live/dead fluorescence images (n = 3). (f) CCK8 assay for cell viability. ** indicates statistical significance at $p < 0.01$ (n = 5). Abbreviations: CCK8: Cell counting kit 8; n.s.: Non-significant.

the scaffolds with three different pore sizes, sectioned the hair follicular hanging drops within the scaffolds, and found that the 1.5 mm pore size group not only matched the size of the hair follicle hanging drops but also displayed normal development and morphology within the scaffold. The 1.2 mm group, due to the overly narrow pores, caused the hair follicular hanging drops to be compressed and deformed within the scaffold. The 1.8 mm group, with pores that were too large, allowed the hair follicular hanging drops to move freely during the preparation of the tissue-engineered skin, thus failing to anchor them in specific areas. In contrast, the 1.5 mm group had a suitable pore size that supported polarized hair follicle growth (Figure 4c).

3.4. 3D-printed degradable hair follicular hanging-drop scaffolds promote *in vitro* hair follicle regeneration

Regeneration of hair follicles *in vitro* was observed only in the 1.5 mm group during the culture of artificially organized skin (Figure 5a). We suspect that this may be related to the polar growth of hair follicles in the 1.5 mm group. Subsequently, the hanging drops were removed, fixed, and sectioned, and the hair follicle-specific markers LHX2 and CK17 were stained using immunohistochemical methods. The immunohistochemical results indicated that both proteins were highly expressed in the hair follicles on the 1.5 mm scaffold (Figure 5b). LHX2 and CK17 are key regulators of hair follicle cycling and differentiation. The expression of these proteins signifies the functional state of the hair follicles, and their presence is crucial for the physiological processes of hair follicle morphology and function.[37–39] Moreover, these results suggest that the mechanical and biochemical properties of the scaffold can have a beneficial impact on the molecular pathways during hair follicle development.

3.5. Collagen signaling regulates dermal–epidermal interactions and drives hair follicle polarity

Since tissue-engineered skin has similar follicle polarization growth as normal skin, we further investigated the underlying mechanisms in normal skin and tried to find a relationship between the two. Previous studies have identified embryonic day 13.5 (E13.5) as a critical stage in hair follicle placode formation, while embryonic day 14.5 (E14.5) marks the emergence of the dermal condensate (DC). This emergence is accompanied by notable morphological changes in basal epithelial cells and the downward invagination of the placode. As this invagination deepens, it converges with the hair follicle dermal papilla (DP), derived from the DC, to form the mature hair follicle structure.[22,40] During this process, interactions between dermal fibroblasts, DC cells, and basal epithelial cells are crucial in directing hair follicle growth. To understand the mechanisms underlying this process, we conducted bioinformatic analyses of single-cell RNA sequencing (scRNA-seq) data from mouse embryonic skin at E13.5 and E14.5 (GSE122043).

Using unsupervised clustering with Seurat, we categorized the cells into 14 clusters based on global gene expression patterns (Figure S1a, Supporting Information). These clusters were assigned to 11 main cell types: basal epithelial cells, suprabasal epithelial cells, fibroblasts, vascular endothelial cells, melanocytes, macrophages, mast cells, myocytes, neurons, vascular smooth muscle cells (VSMC), and DC cells (Figure 6a). Importantly, DC cells emerged at E14.5, representing a pivotal event in hair follicle development. Marker genes were identified for each cell type: *Col1a1* and *Pdgfra* for fibroblasts, *Krt14* and *Krt5* for basal epithelial cells, *Tyr* and *Dct* for melanocytes, and *Bmp4* and *Fgf10* for DC cells (Figure 6b). These marker genes further validated the biological identities of the identified populations and their roles in skin and hair follicle morphogenesis.

Furthermore, cell type proportions exhibited dynamic changes between E13.5 and E14.5, with a reduction in fibroblasts and an expansion of basal and suprabasal epithelial cells. Notably, the appearance of DC cells at E14.5 highlighted the cellular reorganization essential for skin development (Figure 6c). To investigate this cellular reorganization in greater detail, we performed CellChat analysis. The results displayed a significant increase in both the number and strength of interactions at E14.5 compared to E13.5 (Figure 6d). Heatmap comparisons demonstrated enhanced interactions involving basal epithelial cells, fibroblasts, and DC cells, with the latter exhibiting the most significant increases, thereby emphasizing their key role in initiating hair follicle development (Figure 6e). Since DC cells are absent at E13.5, a separate analysis of cell–cell interactions was conducted at E14.5. In this analysis, fibroblasts were identified as the predominant signal senders, targeting basal epithelial cells as primary signal receivers. DC cells acted as both active senders and receivers, further highlighting their central role in dermal–epidermal communication (Figures 6f and S1b, Supporting Information). Taken together, these findings suggest that fibroblasts and DC cells collaborate to guide basal epithelial cell behavior during hair follicle formation.

In addition, pathway analysis revealed significant upregulation of the Collagen signaling pathway at E14.5, which likely drives basal epithelial cell development, thereby establishing the polarity required for hair follicle

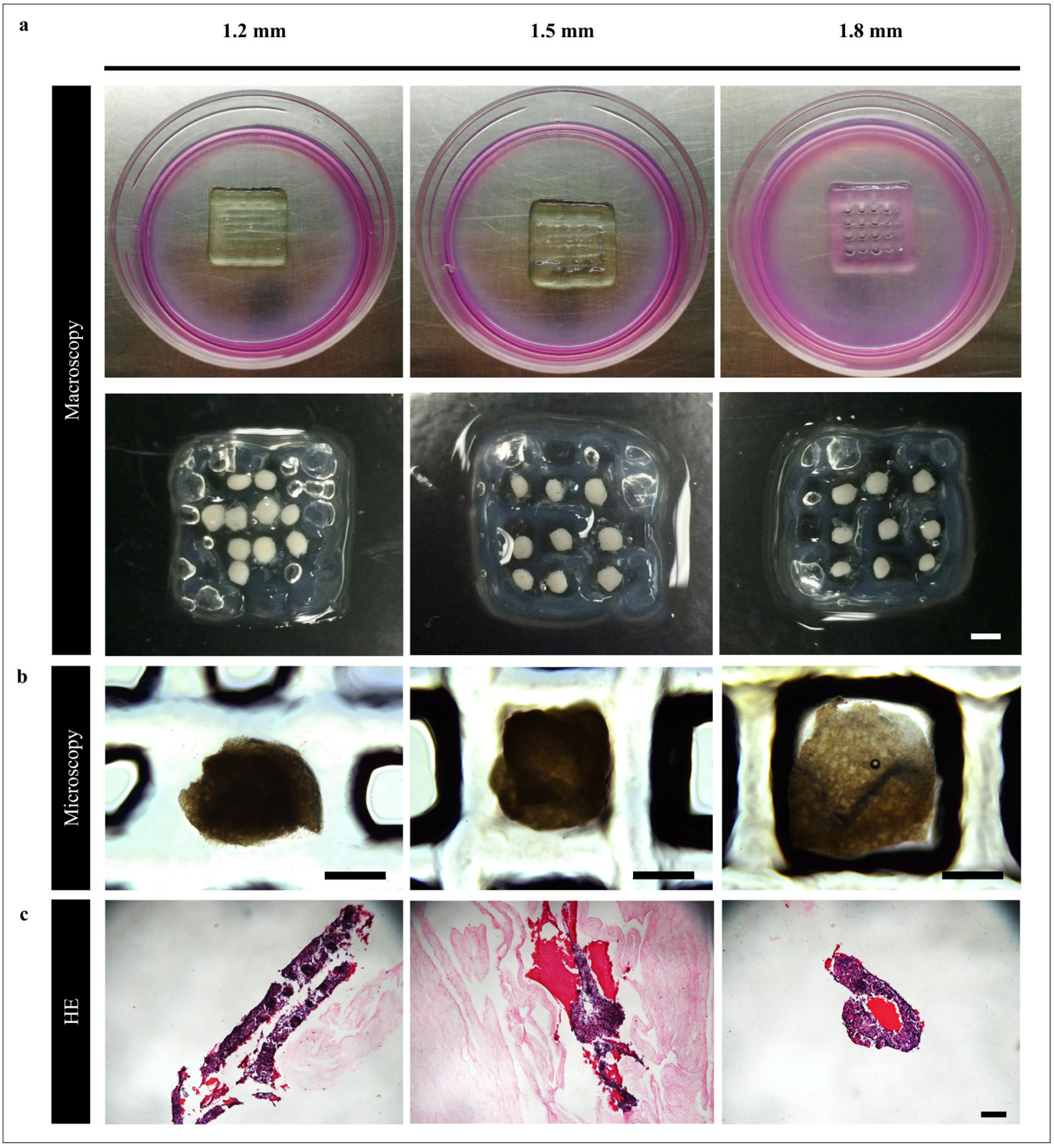

Figure 4. Incorporation of guiding lattice and hair follicular hanging drops. (a) Macroscopic images of 3D-printed degradable hair follicular hanging-drop scaffolds. (b) Microscopic structural images of 3D-printed degradable hair follicular hanging-drop scaffolds. (c) Hematoxylin and eosin (HE) staining of 3D-printed degradable hair follicular hanging-drop scaffolds. Scale bars: 2 mm (a); 500 μm (b); 1 mm (c).

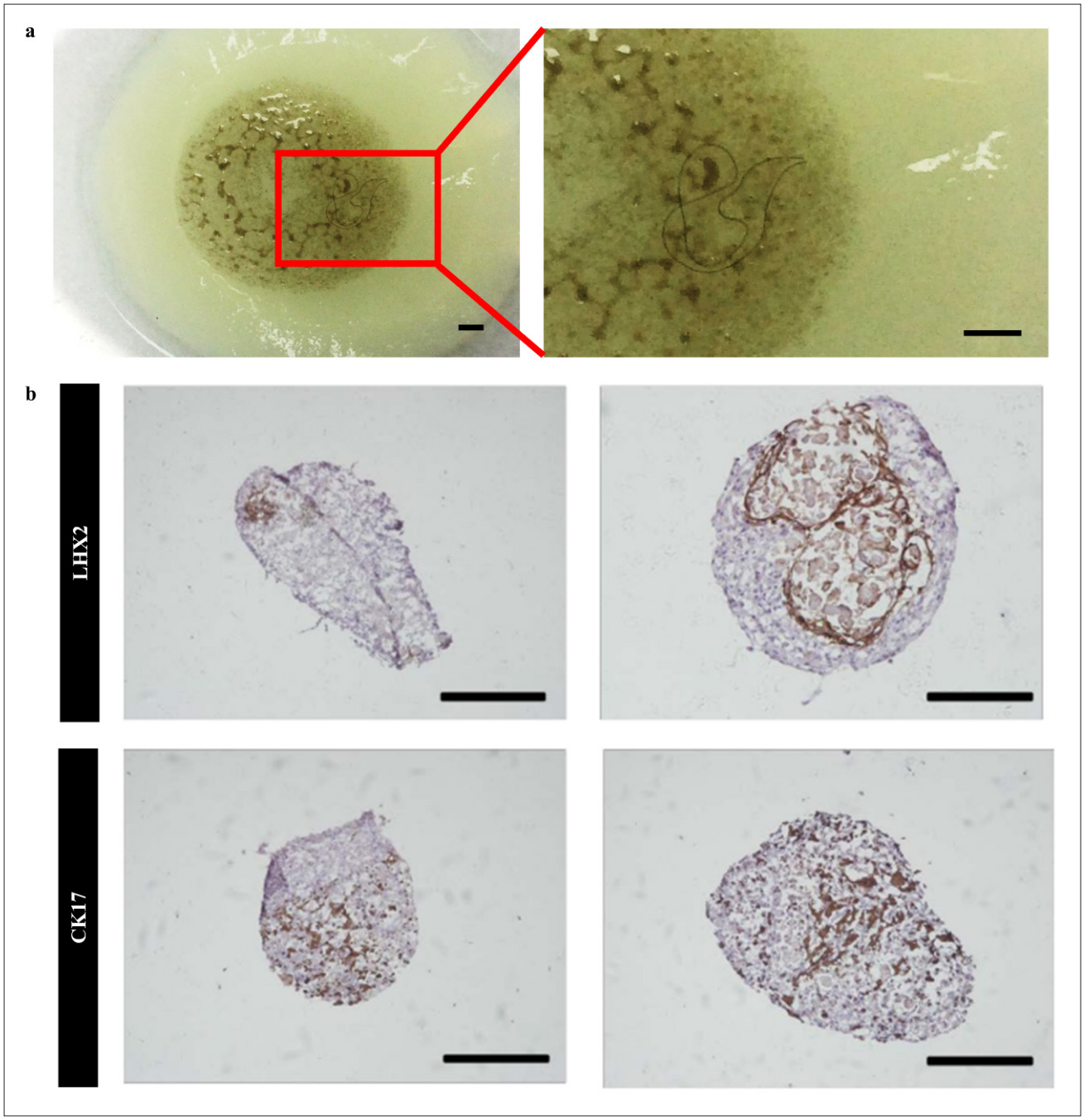

Figure 5. Schematic overview of the tissue-engineered skin and immunohistochemical staining of hair follicular hanging drop-specific markers. (a) Macroscopic images of tissue-engineered skin in the 1.5 mm group. (b) Immunohistochemical staining of hair follicles. Scale bars: 2 mm (a); 200 μm (b).

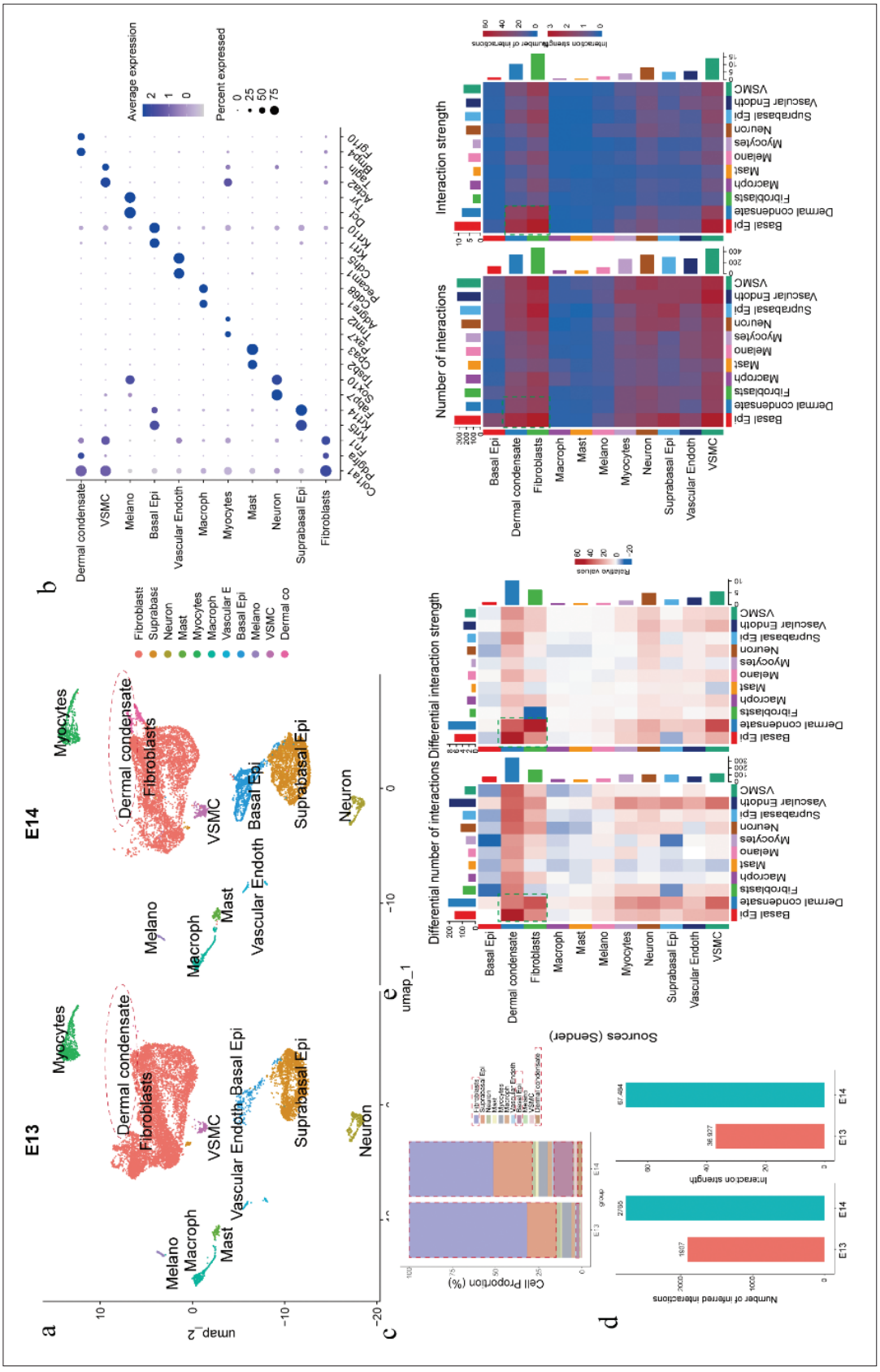
a
E13
E14
Myocytes
Dermal condensate
Fibroblasts
VSMC
Vascular Endoth
Basal Epi
Suprabasal Epi
Neuron
Melano
Macroph
Mast
umap_1
umap_2
b
Average expression
Percent expressed
Dermal condensate
VSMC
Melano
Basal Epi
Vascular Endoth
Macroph
Myocytes
Mast
Neuron
Suprabasal Epi
Fibroblasts
Col1a1
Pdgfra
Fn1
Krt5
Krt14
Fabp7
Sox10
Tpsb2
Cd34
Pax7
Tmtl2
Adgre1
Pecam1
Cdh5
Krt1
Krt10
Dct
Tyr
Acta2
Ascl3
Bpifa1
Ppp1r1b
c
Cell Proportion (%)
d
Number of inferred interactions
Interaction strength
e
Differential number of interactions
Differential interaction strength
Relative values
Sources (Sender)
Targets (Receiver)
Number of interactions
Interaction strength
Basal Epi
Dermal condensate
Fibroblasts
Macroph
Mast
Melano
Myocytes
Neuron
Suprabasal Epi
Vascular Endoth
VSMC

Figure 6.

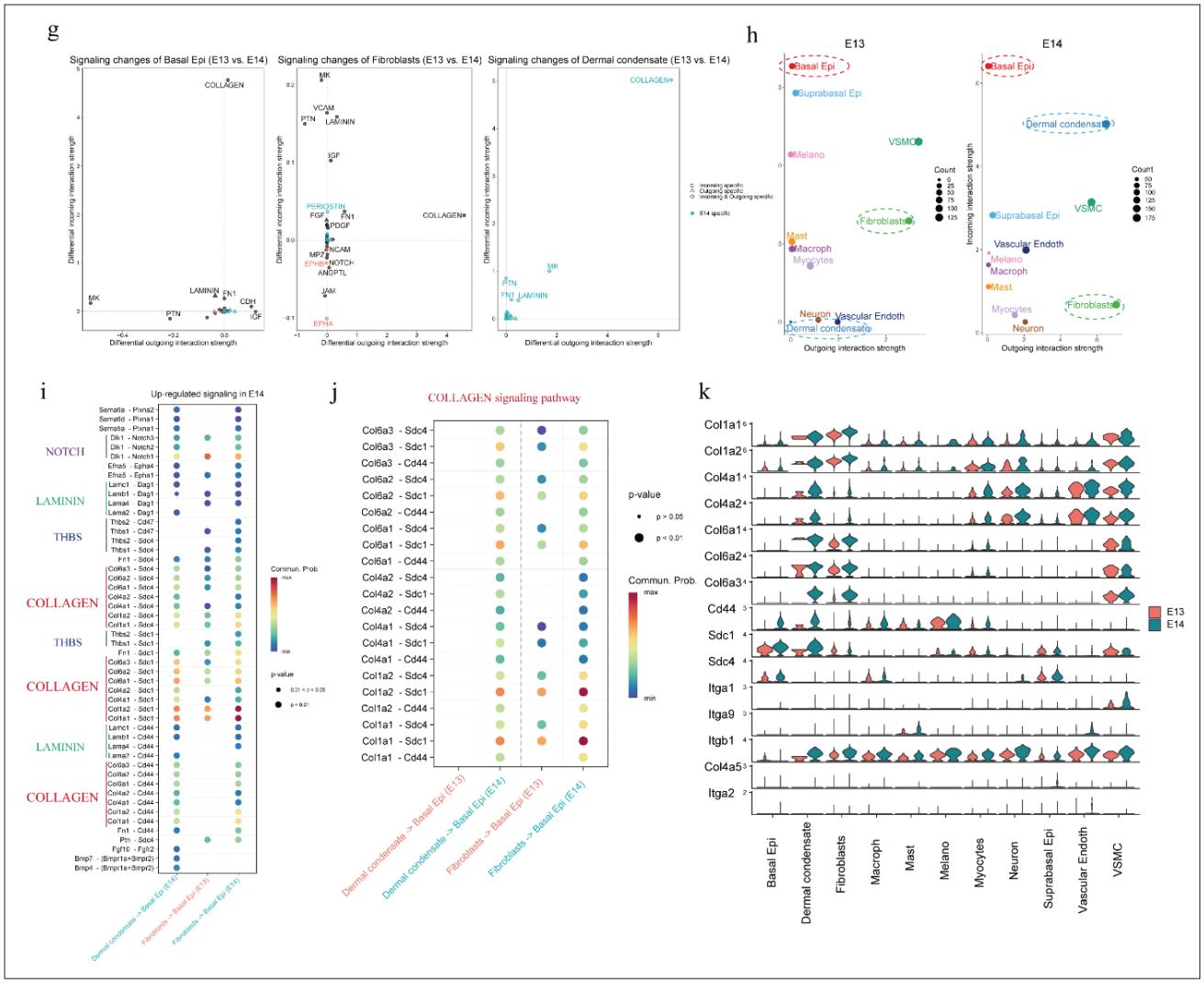

Figure 6. Single-cell RNA sequencing analysis of mouse embryonic skin. (a) Uniform Manifold Approximation and Projection (UMAP) plots demonstrating the cell types of single-cell RNA sequencing data derived from mouse embryonic skin at E13.5 (left, E13) and E14.5 (right, E14). (b) Dot plot displaying the expression of different cell type-specific marker genes, used to annotate the cell types. Dot size indicates the percentage of cells expressing the gene; color represents averaged scaled expression (lavender: low; blue: high). (c) Stacked bar plots of the proportion (*y*-axis) of different cell types from E13.5 and E14.5. (d) Bar plots comparing the number (left) and strength (right) of inferred cell–cell interactions in mouse embryonic skin at E13.5 and E14.5. (e) Heatmaps of differential interaction numbers (left) and strengths (right) between E13.5 and E14.5. Red indicates increased interactions; blue indicates decreased interactions. (f) Heatmaps of cell–cell interaction numbers (left) and strengths (right) at E14.5 across all cell types. (g) Differential outgoing (*x*-axis) and incoming (*y*-axis) interaction strengths for signaling pathways in basal epithelial cells (left), fibroblasts (middle), and DC cells (right) between E13.5 and E14.5. (h) Scatter plots of outgoing (*x*-axis) and incoming (*y*-axis) interaction strengths in the GOLLAGEN pathway for each cell type at E13.5 (left) and E14.5 (right). Circle size represents the number of interactions. (i) Dot plot of upregulated signaling pathways from DC cells (blue) and fibroblasts (orange) to basal epithelial cells at E14.5. Dot size represents statistical significance (*p*-value), and color indicates communication probability. (j) Dot plot of receptor–ligand pairs in the COLLAGEN pathway from DC cells and fibroblasts to basal epithelial cells at E13.5 and E14.5. (k) Violin plots of ligand (e.g., *Col1a1, Col4a1*) and receptor (e.g., *Sdc1, Cd44*) expression levels across cell types at E13.5 (red) and E14.5 (blue). Abbreviations: Basal Epi, basal epithelial cells; DC, dermal condensate; Macroph, macrophages; Melano, melanocytes; Suprabasal epi, suprabasal epithelial cells; vascular endoth, vascular endothelial cells; VSMC, vascular smooth muscle cells.

morphogenesis. Moreover, additional pathways, such as Laminin and NOTCH were also differentially activated, further supporting the hypothesis that coordinated dermal–epidermal signaling shapes hair follicle development (Figures 6g and h and S1c–f, Supporting Information). To gain deeper insights into these pathways, we analyzed upregulated pathways and identified significant enrichment of the COLLAGEN pathway (**Figure 6i**). Specifically, receptor–ligand pairs, such as *Col1a1-Sdc1*, *Col6a2-Cd44*, and *Col4a1-Sdc4*, were prominently upregulated, highlighting their roles in mediating dermal–epidermal interactions (Figures 6j and S1g, Supporting Information). For example, *Sdc1*, expressed primarily in basal epithelial cells, was identified as a key receptor for multiple ligands, facilitating basal epithelial cell migration. Furthermore, expression analysis confirmed significant upregulation of collagen-related ligands (*Col1a1, Col6a2, Col4a1*) and receptors (*Sdc1, Cd44, Sdc4*) in basal epithelial cells, fibroblasts, and DC cells at E14.5 (Figure 6k). Collectively, these findings demonstrate that the upregulation of COLLAGEN signaling at E14.5 promotes dermal–epidermal interactions, ultimately driving the downward development of the hair follicle placode and establishing the growth polarity essential for hair follicle morphogenesis.

4. Conclusion

In this study, we utilized 3D printing technology to construct a lattice structure for the growth and development of hair follicles. It not only provides horizontal support for hair follicular hanging drops but also ensures precise positioning for hair follicle implantation. By regulating the degradation rate and pore size of the lattice, we identified the optimal microenvironment for hair follicle growth and development, avoiding the rupture of hair follicles due to overly small scaffold pores or the inability to guide hair follicle growth due to overly large pores. After integration into tissue-engineered skin, we observed the regeneration of hair follicles *in vitro*. Hematoxylin and eosin section staining demonstrated follicular polar growth similar to normal skin. Through immunohistochemical sectioning, we also noted high expression of hair follicle-specific markers LHX2 and CK17. Furthermore, we found that the growth polarity required for hair follicle morphogenesis is due to the upregulation of COLLAGEN signaling at E14.5, which promotes dermal–epidermal interactions. Hair follicle polarization on 3D-printed scaffolds may also be related to COLLAGEN signaling.

Meanwhile, this study has several limitations. Our experiments primarily focused on scaffold degradation and pore size, lacking a comprehensive evaluation of mechanical properties—including stiffness, surface roughness, and elasticity—which may also influence hair follicle growth and polarity. Furthermore, while the current findings are based on *in vitro* models, we fully acknowledge the necessity of animal studies to validate scaffold performance in more complex biological environments. As a next step, we plan to conduct *in vivo* experiments to assess the long-term effects of the scaffold, including its biocompatibility and functional integration within living systems.

In summary, the combination of 3D printing and hair follicular hanging-drop technology offers a new perspective for hair follicle regeneration and application, filling the gap in the implantation of hair follicles in tissue-engineered skin and providing a novel strategy for the establishment of fully functional artificial skin.

Acknowledgments

None.

Funding

This research was funded by the National Natural Science Foundation of China (NSFC) (82170256), the Guangdong Major Project of Basic and Applied Basic Research (2023B0303000005), and the Guangdong Provincial Special Support Program for Prominent Talents (2021JC06Y656).

Conflict of interest

The authors declare that they have no known competing financial interests or personal relationships that could have appeared to influence the work reported in this paper.

Author contributions

Conceptualization: Bin Yao, Yuhong Wang, Dongzhen Zhu
Data curation: Bin Yao, Yuhong Wang, Dongzhen Zhu
Funding acquisition: Sha Huang, Ping Zhu
Investigation: Bin Yao, Yuhong Wang, Dongzhen Zhu
Methodology: Tian Huang
Software: Tian Huang
Validation: Bin Yao, Yuhong Wang, Dongzhen Zhu
Visualization: Bin Yao, Yuhong Wang, Dongzhen Zhu
Writing – original draft: Bin Yao, Yuhong Wang, Dongzhen Zhu
Writing – review & editing: Bin Yao, Yuhong Wang, Dongzhen Zhu, Sha Huang, Ping Zhu

Ethics approval and consent to participate

The experimental animals used in this study were reviewed and approved by the Animal Ethics Committee of Tianjin University (TJUE-2024-515), ensuring full compliance with animal protection, welfare, and ethical principles, as

well as the relevant national regulations on animal welfare and ethics.

Consent for publication

Not applicable.

Availability of data

Data is available from the corresponding author upon reasonable request.

References

1. Singer AJ, Dagum AB. Current management of acute cutaneous wounds. *N Engl J Med*. 2008;359(10):1037-1046. doi: 10.1056/NEJMra0707253
2. Hall J, Buckley HL, Lamb KA, et al. Point prevalence of complex wounds in a defined United Kingdom population. *Wound Repair Regen*. 2014;22(6):694-700. doi: 10.1111/wrr.12230
3. Jiang Y, Huang S, Fu X, et al. Epidemiology of chronic cutaneous wounds in China. *Wound Repair Regen*. 2011;19(2):181-188. doi: 10.1111/j.1524-475X.2010.00666.x
4. Kabashima K, Honda T, Ginhoux F, et al. The immunological anatomy of the skin. *Nat Rev Immunol*. 2019; 19(1):19-30. doi: 10.1038/s41577-018-0084-5
5. Baker LB. Physiology of sweat gland function: the roles of sweating and sweat composition in human health. *Temperature (Austin)*. 2019;6(3):211-259. doi: 10.1080/23328940.2019.1632145
6. Sierra-Sánchez Á, Kim KH, Blasco-Morente G, et al. Cellular human tissue-engineered skin substitutes investigated for deep and difficult to heal injuries. *NPJ Regen Med*. 2021;6(1):1-23. doi: 10.1038/s41536-021-00144-0
7. Sierra-Sánchez Á, Fernández-González A, Lizana-Moreno A, et al. Hyaluronic acid biomaterial for human tissue-engineered skin substitutes: preclinical comparative in vivo study of wound healing. *J Eur Acad Dermatol Venereol*. 2020;34(10):2414-2427. doi: 10.1111/jdv.16342
8. Mansbridge JN. Tissue-engineered skin substitutes in regenerative medicine. *Curr Opin Biotechnol*. 2009;20(5):563-567. doi: 10.1016/j.copbio.2009.08.008
9. Nourian Dehkordi A, Mirahmadi Babaheydari F, Chehelgerdi M, et al. Skin tissue engineering: wound healing based on stem-cell-based therapeutic strategies. *Stem Cell Res Ther*. 2019;10(1):111. doi: 10.1186/s13287-019-1212-2
10. Costello L, Dicolandrea T, Tasseff R, et al. Tissue engineering strategies to bioengineer the ageing skin phenotype in vitro. *Aging Cell*. 2022;21(2):e13550. doi: 10.1111/acel.13550
11. Chen J, Fan Y, Dong G, et al. Designing biomimetic scaffolds for skin tissue engineering. *Biomater Sci*. 2023;11(9):3051-3076. doi: 10.1039/d3bm00046j
12. Amirsadeghi A, Jafari A, Eggermont LJ, et al. Vascularization strategies for skin tissue engineering. *Biomater Sci*. 2020;8(15):4073-4094. doi: 10.1039/d0bm00266f
13. Bock O, Schmid-Ott G, Malewski P, et al. Quality of life of patients with keloid and hypertrophic scarring. *Arch Dermatol Res*. 2006;297(10):433-438. doi: 10.1007/s00403-006-0651-7
14. Lei M, Schumacher LJ, Lai Y-C, et al. Self-organization process in newborn skin organoid formation inspires strategy to restore hair regeneration of adult cells. *Proc Natl Acad Sci U S A*. 2017;114(34):E7101-E7110. doi: 10.1073/pnas.1700475114
15. Abaci HE, Coffman A, Doucet Y, et al. Tissue engineering of human hair follicles using a biomimetic developmental approach. *Nat Commun*. 2018;9(1):5301. doi: 10.1038/s41467-018-07579-y
16. Huang S, Xu Y, Wu C, et al. In vitro constitution and in vivo implantation of engineered skin constructs with sweat glands. *Biomaterials*. 2010;31(21):5520-5525. doi: 10.1016/j.biomaterials.2010.03.060
17. Huang S, Yao B, Xie J, et al. 3D bioprinted extracellular matrix mimics facilitate directed differentiation of epithelial progenitors for sweat gland regeneration. *Acta Biomater*. 2016;32:170-177. doi: 10.1016/j.actbio.2015.12.039
18. Kang MS, Kwon M, Park R, et al. Harnessing the intradermal delivery of hair follicle dermal papilla cell spheroids for hair follicle regeneration in nude mice. *Biomater Res*. 2025;29:0129. doi: 10.34133/bmr.0129
19. Zheng Y, Du X, Wang W, et al. Organogenesis from dissociated cells: generation of mature cycling hair follicles from skin-derived cells. *J Invest Dermatol*. 2005;124(5):867-876. doi: 10.1111/j.0022-202X.2005.23716.x
20. Wang Y, Liu T, Guo Y, et al. Integrating melt electrospinning writing and microfluidics to engineer a human cardiac microenvironment for high-fidelity drug screening. *Bioact Mater*. 2025;45:551-566. doi: 10.1016/j.bioactmat.2024.11.037
21. Carlson MW, Alt-Holland A, Egles C, et al. Three-dimensional tissue models of normal and diseased skin. *Curr Protoc Cell Biol*. 2008, Chapter 19: Unit 19.9. doi: 10.1002/0471143030.cb1909s41

22. Gupta K, Levinsohn J, Linderman G, et al. Single-cell analysis reveals a hair follicle dermal niche molecular differentiation trajectory that begins prior to morphogenesis. *Dev Cell*. 2019;48(1):17-31.e6.
doi: 10.1016/j.devcel.2018.11.032

23. Lin B, Miao Y, Wang J, et al. Surface tension guided hanging-drop: producing controllable 3D spheroid of high-passaged human dermal papilla cells and forming inductive microtissues for hair-follicle regeneration. *ACS Appl Mater Interfaces*. 2016;8(9):5906-5916.
doi: 10.1021/acsami.6b00202

24. Kalabusheva E, Terskikh V, Vorotelyak E. Hair germ model in vitro via human postnatal keratinocyte-dermal papilla interactions: impact of hyaluronic acid. *Stem Cells Int*. 2017;2017:9271869.
doi: 10.1155/2017/9271869

25. Wang J, Liu S, Huang J, et al. Alginate: microbial production, functionalization, and biomedical applications. *Int J Biol Macromol*. 2023;242:125048.
doi: 10.1016/j.ijbiomac.2023.125048

26. Hecht H, Srebnik S. Structural characterization of sodium alginate and calcium alginate. *Biomacromolecules*. 2016;17(6):2160-2167.
doi: 10.1021/acs.biomac.6b00378

27. Mallakpour S, Mohammadi N. Development of sodium alginate-pectin/TiO2 nanocomposites: antibacterial and bioactivity investigations. *Carbohydr Polym*. 2022;285:119226.
doi: 10.1016/j.carbpol.2022.119226

28. Sanchez-Ballester NM, Bataille B, Soulairol I. Sodium alginate and alginic acid as pharmaceutical excipients for tablet formulation: structure-function relationship. *Carbohydr Polym*. 2021;270:118399.
doi: 10.1016/j.carbpol.2021.118399

29. Do UT, Kim J, Luu QS, et al. Accurate detection of enzymatic degradation processes of gelatin–alginate microcapsule by 1H NMR spectroscopy: probing biodegradation mechanism and kinetics. *Carbohydr Polym*. 2023;304:120490.
doi: 10.1016/j.carbpol.2022.120490

30. Chen C, Li X, Lu C, et al. Advances in alginate lyases and the potential application of enzymatic prepared alginate oligosaccharides: a mini review. *Int J Biol Macromol*. 2024;260:129506.
doi: 10.1016/j.ijbiomac.2024.129506

31. Ma J, Qin C, Wu J, et al. 3D multicellular micropatterning biomaterials for hair regeneration and vascularization. *Mater Horiz*. 2023;10(9):3773-3784.
doi: 10.1039/d3mh00528c

32. Motter Catarino C, Cigaran Schuck D, Dechiario L, et al. Incorporation of hair follicles in 3D bioprinted models of human skin. *Sci Adv*. 2023;9(41):eadg0297.
doi: 10.1126/sciadv.adg0297

33. Yao B, Hu T, Cui X, et al. Enzymatically degradable alginate/gelatin bioink promotes cellular behavior and degradation in vitro and in vivo. *Biofabrication*. 2019;11(4):045020.
doi: 10.1088/1758-5090/ab38ef

34. Lee JJ, Lee S-G, Park JC, et al. Investigation on biodegradable PLGA scaffold with various pore size structure for skin tissue engineering. *Curr Appl Phys*. 2007;7:e37-e40.
doi: 10.1016/j.cap.2006.11.011

35. Zhang Z, Feng Y, Wang L, et al. A review of preparation methods of porous skin tissue engineering scaffolds. *Mater Today Commun*. 2022;32:104109.
doi: 10.1016/j.mtcomm.2022.104109

36. Han J, Wu J, Xiang X, et al. Biodegradable BBG/PCL composite scaffolds fabricated by selective laser sintering for directed regeneration of critical-sized bone defects. *Mater Design*. 2023;225:111543.
doi: 10.1016/j.matdes.2022.111543

37. Cao M, Zhao J, Du L, et al. The combination of hair follicle-specific marker LHX2 and co-expressed marker can distinguish between sweat gland placodes and hair placodes in rat. *J Mol Histol*. 2021;52(6):1225-1232.
doi: 10.1007/s10735-021-10023-z

38. Tomann P, Paus R, Millar SE, et al. Lhx2 is a direct NF-κB target gene that promotes primary hair follicle placode down-growth. *Development*. 2016;143(9):1512-1522.
doi: 10.1242/dev.130898

39. Rhee H, Polak L, Fuchs E. Lhx2 maintains stem cell character in hair follicles. *Science*. 2006;312(5782):1946-1949.
doi: 10.1126/science.1128004

40. Villeneuve C, Hashmi A, Ylivinkka I, et al. Mechanical forces across compartments coordinate cell shape and fate transitions to generate tissue architecture. *Nature Cell Biol*. 2024;26(2):207-218.
doi: 10.1038/s41556-023-01332-4